Chapter 7

Impact of dilating forcing amplitudes on peristaltically driven non-Newtonian fluid in an elastic tube: Application to swallowing disorder

7.1 Introduction

A flexible tube allows a circumferential movement along it, which results in the physiological process known as peristalsis. Peristalsis helps in the fluid movement within living organisms, which is of paramount importance. Circulation of the blood in the heart-lung machine is just one example of the many mechanical systems created to transfer fluids using the peristaltic pumping concept. The material's ability to stretch and return to its original shape, its innate resistance to deformation, allows

The content of this chapter is published in Zeitschrift für Naturforschung A (ZNA) 79(09) (2024). DOI: doi.org/10.1515/zna-2024-0063

it to promptly revert to its original form once the deforming force is eliminated. A comprehensive understanding of the underlying mechanisms is imperative to comprehend the intricate processes involved in viscous flow within elastic tubes. This knowledge holds great significance in medicine, biology, biomedical technology, and industry, particularly in applications such as artery grafting, atherosclerosis, and facilitating bolus transport in the esophagus. The insights into the mechanisms governing the transportation of food and liquids through the esophagus and intestines are crucial for effectively managing patients with transport disorders. It's important to note that the physiology of these processes remains intricate and not entirely elucidated. Existing models for biological ducts often lack comprehensive discussions regarding the solid mechanics of tube walls, muscle contractions, and material stiffness, among other factors. To ensure accurate modeling, it is essential to consider the deformable boundary's shape in tube mechanics. Furthermore, investigations into peristalsis within elastic tubes are anticipated to yield valuable insights for developing prosthetic limbs.

Solving the mathematics, which involved the terms for modeling biological organs and even their elastic properties of the tube wall, was never an easy task for the mathematician, especially in getting the exact solution for the modeled problem. Researchers such as Fung (1971), Griffiths (1989), Carew and Pedley (1997) treated the problem of the dynamics of the ureter. In summary, Fung and Yih (1968) focused on ureteral peristalsis driven explicitly by muscle contractions. His findings emphasized the significance of a substantial reserve of muscle tension behind the bolus, ensuring a secure closure that guarantees complete fluid removal with each bolus passage. As the bolus reaches the ureterovesical junction, resistance to its motion increases, and the reserve tension becomes crucial for pushing urine into the bladder via the junction.

Griffiths (1989) concluded that effective pumping by the ureteral peristaltic contractions is limited at higher mean flow rates, and in some cases, these contractions may even impede urine flow. Thus, the peristaltic pump operates optimally in situations with a reduced flow rate and pressure.

Wong and Rautaharju (1968) and Sandler and Dodge (1963) treated the heart as an isotropic elastic body. Young (1832) commenced the evaluation of the significance of elasticity in the pulse wave generated by the heart. Rubinow and Keller

(1972), in conjunction with Fung and Fung (1997), explored local Poiseuille's flow and established that the tube radius can be ascertained by the equilibrium between transmural pressure and the tension in the tube wall.

Rubinow and Keller (1972) delved into the movement of a viscous fluid within a flexible tube and found that knowing the cross-sectional shape allows the determination of tube conductivity by solving an appropriate flow problem. They also noted that conductivity diminishes with the reduction in pressure disparity between the tube's inside and outside increases.

The circulatory system, an intricate network of elastic tubes with branches, was modeled by Takagi and Balmforth (2011) using linear elasticity for tube wall deformation and the lubrication approximation for internal flow. The investigation of the fluid flow through a finite length, axisymmetric tube when the elastic wall is subject to either a prescribed external pressure or a prescribed motion was done by Waters and Guiot (2001). They assumed that the prescribed forcing on the wall consisted of a peristaltic wave propagated forward together with their reflection to the backward. This resulted in an increase in the mean flow rate as the degree of wave reflection increases. Meanwhile, wave reflection also leads to a reduction in the mean flow rate when it is subjected to the movement of the wall. However, the study of the two different types of fluid in a tube of an elastic in nature has been investigated by Sochi (2014). He demonstrated qualitative similarities and asymptotic reductions in his considered governing equations of the flow of different scenarios.

Uddin et al. (2018) examined the transportation of a nano-fluid using bio-elastic sheets, examining scenarios with stretched, stationary, and shrinking sheets, as well as slip and no-slip conditions, revealing changes in heat transfer rates with thermophoresis and buoyancy ratio parameters.

Some researchers have considered the non-Newtonian nature of fluids, such as Selvi et al. (2018), who analyzed blood flow in elastic arteries using a power-law fluid model. They found that flow as a function of intake and outlet pressure exhibited distinct behaviors. Additionally, Selvi and Srinivas (2018) explored the pulsatile flow of a conducting Jeffrey fluid through a porous elastic tube with variable cross-section, highlighting velocity distribution patterns.

Hayat et al. (2018) conducted an analysis of the magnetohydrodynamic peristaltic flow of a Prandtl fluid in a channel with flexible walls, observing changes in axial velocity, temperature, and heat transfer coefficient with variations in the Prandtl fluid parameter. Despite considerable research in this area, a deeper understanding of the genuine implications of the elastic properties of vessels remains relatively limited.

Recent studies on non-Newtonian fluid with applications in physiology, especially for blood flow, have been done by researchers such as Sharma et al. (2017), Sharma and Yadav (2019), Jaiswal and Yadav (2019), Yadav et al. (2020), Pandey and Yadav (2022), Yadav and Yadav (2023a), Yadav and Yadav (2023b), Yadav and Roshan (2024), Yadav and Yadav (2024).

Recently, Rosti and Takagi (2021) investigated the rheology of a two-fluid emulsion under semi-concentrated conditions. Their study considered a solute with Newtonian rheology and a solvent with inelastic power-law behavior. Their findings suggest that the variations in emulsion viscosity primarily arise from changes in the coalescence phenomenon within the system. Specifically, they noted that modifying the properties of the carrier fluid led to significant effects. In the case of shear-thickening fluids, local regions between interacting droplets exhibited high shear rates, resulting in an increase in local viscosity. Conversely, these regions exhibited low shear rates for shear-thinning fluids, leading to a reduction in local viscosity. These variations ultimately influenced the drainage time of the entire system.

Tripathi et al. (2022) delve into a mathematical model concerning non-Newtonian fluid behavior, investigating its implications on the thermal aspects of SARS-CoV-2 transmission within the peristaltic blood flow. Their findings suggest that micro-droplets carry fewer coronavirus particles, thereby mitigating the severity of airborne infections. Inspired by the burgeoning field of microfluidics, Bhandari et al. (2022) explore a mathematical framework describing the dynamics of unsteady viscous flow in microchannels subjected to periodic membrane pumping, modulated by electromagnetohydrodynamics. Additionally, Tripathi et al. (2023), Bhardwaj et al. (2024), and Bhandari et al. (2024) conduct studies on micro-scale pumping dynamics, alterations in electro-osmotic flow through membrane microchannels (exhibiting non-Newtonian behavior), and parametric analyses of multi-membrane-based pumping flow models with induced magnetic fields, respectively.

The study related to the transportation of food bolus into the oesophagus considering different fluids, such as Newtonian and non-Newtonian, for various geometries was carried out by researchers such as Li and Brasseur (1993), Misra and Pandey (2001), and Misra and Maiti (2012b). However, the finding related to the wave amplitude dilation, which enhances the pressure at the lower end of the oesophagus, was incorporated by Pandey et al. (2017). This finding opened a new gateway to the model that has been further presented by Pandey and Singh (2019) and Pandey et al. (2018), and Pandey and Pandey (2024a) for the case of non-Newtonian flows in the oesophagus.

Additionally, Pandey and Singh (2018) explored the impact of suspended particles on oesophageal swallowing. In contrast, in another study, Pandey and Singh (2019) investigated oesophageal flow in the presence of a hiatus hernia using the same approach. Besides, the model considering the elasticity property of the oesophageal wall was presented by Pandey and Singh (2020) for Newtonian fluids. A comprehensive examination of the available literature underlines the significant need for flow models incorporating non-Newtonian fluids within the context of elastic tubes representing the oesophageal wall. Our study in the present article is focused on evaluating the characteristics like pressure, velocity, and stream functions for sinusoidal wave forcing and solitary wave with Gaussian forcing for fluids of a non-Newtonian nature. Apart from these objectives, we are also looking for answers to a few questions that follow:

(i) What will be the result of the impacts of dilating forcing amplitudes on pressure distribution along the axial length of an elastic oesophageal tube due to the sinusoidal wave forcing?

(ii) Does the transition from pseudoplasticity to dilatancy of the fluid require more pressure to propel the boluses toward the cardiac sphincter?

(iii) What will happen with the axial velocity profile on decreasing the flow behavior index? Will the trends be the opposite in the case of dilatant fluid?

(iv) Will there be any attenuation or enhancement in the magnitude of radial velocity due to the shear thickening or thinning of the fluids?

7.2 Mathematical formulation

We present the model of the peristaltic transport in an elastic oesophageal tube, which is considered as a circular cylindrical tube of radius a (when the tube is static) carrying a power-law fluid. The tube experiences a force $F_e(z - ct)$ in the radially inward direction on its boundary (Figure 7.1). The elastic oesophageal tube wall is subjected to the periodic peristaltic movement with speed c, amplitude ϕ, and wavelength λ, and its instantaneous radius at any axial direction z is given by $r = h(z, t)$.

We use the non-dimensional variables (Pandey et al. (2011))
$h = \frac{\tilde{H}}{a}$, $t = \frac{c\tilde{t}}{\lambda}$, $v = \frac{\tilde{v}}{\delta c}$, $r = \frac{\tilde{r}}{a}$, $k = \frac{\tilde{k}}{\lambda}$, $p = \frac{\tilde{p}a^{n+1}}{\lambda\mu c^n}$, $L = \frac{\tilde{L}}{\lambda}$, $z = \frac{\tilde{z}}{\lambda}$, $\phi = \frac{\tilde{\phi}}{a}$, $u = \frac{\tilde{u}}{c}$, where, $\delta = \frac{a}{\lambda}$, and L are wave number and oesophageal length respectively. Here, the given symbols such as r, z, t, k, u, v, and p represent radial direction, axial direction, time, dilating parameter, axial velocity, radial velocity, and pressure, respectively. The left-hand side denotes dimensionless quantities, and the quantities on the right-hand side with ˜ are dimensional variables. In the case of power-law fluid, we use the Reynolds number $R_e = \frac{\rho c^{2-n}a^{n+1}}{\mu\lambda}$, where n is the power-law flow behavior index.

In order to get rid of those terms, which consist of curvature effects and convective inertial forces, by comparing them with the viscous forces, we use the assumptions of the long wavelength and low Reynolds number approximations. With these assumptions, the governing equations are reduced to (Misra and Pandey (2001))

$$\frac{\partial p}{\partial z} = \left(sign\frac{\partial u}{\partial r}\right)\left[\frac{1}{r}\frac{\partial}{\partial r}\left\{r\left|\frac{\partial u}{\partial r}\right|^n\right\}\right], \tag{7.1}$$

$$\frac{\partial p}{\partial r} = 0, \tag{7.2}$$

$$\frac{1}{r}\frac{\partial (rv)}{\partial r} + \frac{\partial u}{\partial z} = 0, \tag{7.3}$$

subject to the boundary conditions are

$$u = 0, \quad at \quad r = h, \tag{7.4}$$

$$v = \frac{\partial h}{\partial t}, \quad at \quad r = h, \tag{7.5}$$

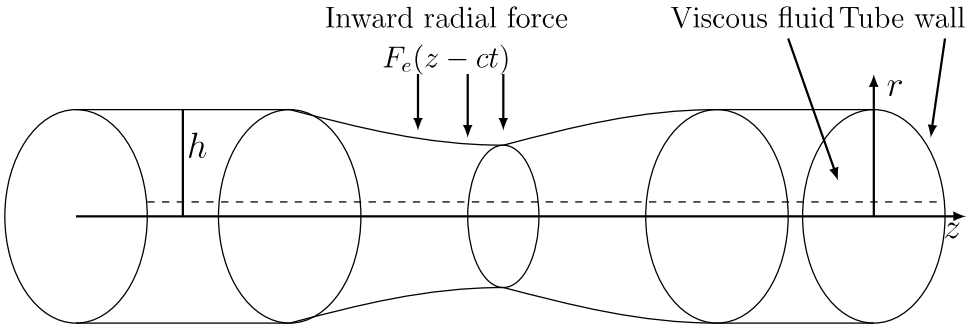

Figure 7.1: Geometry of an elastic tube experienced by inward radial force on its tube wall filled with viscous fluid inside it.

$$v = 0, \frac{\partial u}{\partial r} = 0 \quad at \quad r = 0. \tag{7.6}$$

The above boundary conditions (7.4) to (7.6) are the no-slip condition at the wall, vibration with the transverse velocity at the wall, and in the radial direction, we take velocity gradient as well as velocity at the centre line to be zero respectively. Furthermore, the pressures at the two ends of the oesophagus are $p(0,t)$ and $p(L,t)$.

7.3 Problem analysis

Equations (7.1) and (7.2) under (7.4) gives axial velocity as

$$u = \Big(sign\frac{\partial p}{\partial z}\Big)\Big|\frac{1}{2}\frac{\partial p}{\partial z}\Big|^{\frac{1}{n}}\frac{n}{n+1}\Big(r^{(n+1)/n} - h^{(n+1)/n}\Big), \tag{7.7}$$

while the radial velocity is obtained by using (7.7) into continuity equation (7.3) under the constraint (7.6) at the centre line, which yields

$$v = \Big(sign\frac{\partial p}{\partial z}\Big)\Big|\frac{\partial p}{\partial z}\Big|\frac{h^{1/n}}{2}\frac{\partial h}{\partial z} - \frac{1}{n+1}\Big(\frac{n}{3n+1}r^{(n+1)/n} - \frac{1}{2}h^{(n+1)/n}\Big)\frac{\partial^2 p}{\partial z^2}\frac{r}{2^{1/n}}\Big|\frac{\partial p}{\partial z}\Big|^{1-n/n}. \tag{7.8}$$

The volume flow rate in the wave frame is

$$q = 2\int_0^H URdR. \tag{7.9}$$

We obtained from the above

$$q = -H^2 - \Big(\frac{1}{2}\frac{\partial p}{\partial z}\Big)^{\frac{1}{n}}\Big(\frac{n}{1+3n}\Big)H^{\frac{1+3n}{n}}. \tag{7.10}$$

Using the equation (Takagi and Balmforth (2011))

$p(h,z,t) - p_0 = DL^{\eta}\frac{\partial^{\eta}}{\partial z^{\eta}}(h-R) + F_e,$

we can establish the force equilibrium for the linear elastic tube (i.e., when $\eta = 0$) as follows:

$p = D(H-1) + F_e.$

In this context, we consider that F_e is represented as $\epsilon e^{kz} f(z)$. Therefore, the equation (7.10) becomes:

$$q = -H^2 - \Big(\frac{D}{2}\frac{dH}{dz} + \frac{\epsilon}{2}\frac{d}{dz}(e^{kz}f(z))\Big)^{\frac{1}{n}}\Big(\frac{n}{1+3n}\Big)H^{\frac{1+3n}{n}}, \tag{7.11}$$

we can rewrite it as

$$(-1)^n\Big(\frac{1+3n}{n}\Big)^n(q+H^2)^n = \Big(\frac{D}{2}\frac{dH}{dz} + \epsilon g(z)\Big)H^{1+3n}, \tag{7.12}$$

where $g(z) = \frac{d}{dz}(e^{kz}f(z))$.
By taking $H = 1 + \epsilon H_1 + \epsilon^2 H_2 + o(\epsilon^3)$ and $q = 1 + \epsilon^2 q_2 + o(\epsilon^3)$, using these values, we write from equation (7.12) as

$$\begin{aligned}(-1)^n\Big(\frac{1+3n}{n}\Big)^n(2^n(1+\epsilon(nH_1) + A = \epsilon\Big(\frac{D}{2}\frac{dH_1}{dz} + g(z)\Big)\\ + \epsilon^2\Big(\frac{(3n+1)}{2}DH_1\frac{dH_1}{dz}\\ + \frac{D}{2}\frac{dH_2}{dz} + (3n+1)H_1 g(z)\Big),\end{aligned} \tag{7.13}$$

where $A = \frac{\epsilon^2}{2}(nq_2 + 2nH_2 + n^2H_1) + o(\epsilon^3)))$.
Comparing the coefficients of ϵ and ϵ^2 on the two sides of equation (7.13), we get

$$\epsilon: \quad (-1)^n nH_1\Big(\frac{1+3n}{n}\Big)^n 2^n = \frac{D}{2}\frac{dH_1}{dz} + g(z). \tag{7.14}$$

$$\epsilon^2: \quad (-1)^n\Big(\frac{1+3n}{n}\Big)^n 2^n\Big(\frac{nq_2+2nH_2+n^2H_1}{2}\Big) = \frac{(3n+1)}{2}DH_1\frac{dH_1}{dz}+\frac{D}{2}\frac{dH_2}{dz} + (3n+1)H_1 g(z). \tag{7.15}$$

7.3.1 Forcing with a sinusoidal wave

We consider $f(z) = sin(z)$ for the sake of illustration of periodic waves, i.e., forcing with a sinusoidal wave, and then impose it with the low amplitude solution to the equations (7.14) and (7.15), we get

$$H_1 = C_1 e^{\beta z} + e^{kz}(A\cos z + B\sin z), \tag{7.16}$$

where constants C_1, α, β, A and B are given in appendix.

$$\begin{aligned} H_2 = &-\frac{q_2}{2} - (3n+1){C_1}^2 + C_2 e^{\beta z} - \frac{2(3n+1)\alpha S_1}{D(2k-\beta)}e^{2kz} + C_1\left(\frac{n\alpha}{D}\right)ze^{\beta z} \\ &+ \left(\frac{n\alpha}{D}\right)e^{kz}(P_1\cos z + Q_1\sin z) - (3n+1)\beta e^{2kz}(P_2\cos 2z + Q_2\sin 2z) \\ &- 2(3n+1)C_1\beta e^{(k+\beta)z}(P_3\cos z + Q_3\sin z), \end{aligned} \tag{7.17}$$

where C_2, S_1, P_1, P_2, P_3, Q_1, Q_2 and Q_3 are constants (refer to appendix 7.5). From equations (7.16) and (7.17), we write

$$\begin{aligned} H = &1 + \epsilon(C_1 e^{\beta z} + e^{kz}(A\cos z + B\sin z)) \\ &+ \epsilon^2\Big(- \frac{q_2}{2} - (3n+1){C_1}^2 + C_2 e^{\beta z} - \frac{2(3n+1)\alpha S_1}{D(2k-\beta)}e^{2kz} + C_1\left(\frac{n\alpha}{D}\right)ze^{\beta z} \\ &+ \left(\frac{n\alpha}{D}\right)e^{kz}(P_1\cos z + Q_1\sin z) - (3n+1)\beta e^{2kz}(P_2\cos 2z + Q_2\sin 2z) \\ &- 2(3n+1)C_1\beta e^{(k+\beta)z}(P_3\cos z + Q_3\sin z)\Big). \end{aligned} \tag{7.18}$$

In the laboratory frame, the equation describing the wall of the elastic oesophageal tube can be expressed as follows.

$$\begin{aligned}h(z,t) &= 1+\epsilon(C_1e^{\beta(z-t)}+e^{kz}(A\cos(z-t)+B\sin(z-t)))\\&+\epsilon^2\Big(-\frac{q_2}{2}-(3n+1){C_1}^2+C_2e^{\beta(z-t)}-\frac{2(3n+1)\alpha S_1}{D(2k-\beta)}e^{2k(z-t)}\\&+C_1\left(\frac{n\alpha}{D}\right)(z-t)e^{\beta(z-t)}+\left(\frac{n\alpha}{D}\right)e^{k(z-t)}(P_1\cos(z-t)+Q_1\sin z)\\&-(3n+1)\beta e^{2k(z-t)}(P_2\cos 2(z-t)+Q_2\sin 2(z-t))\\&-2(3n+1)C_1\beta e^{(k+\beta)(z-t)}(P_3\cos(z-t)+Q_3\sin(z-t))\Big).\end{aligned}\tag{7.19}$$

In the laboratory frame, the flow rate in terms of volume is $Q(z,t)=2\int_0^h rudr$. Since the expression for the velocity along the axial length of an elastic oesophageal tube is calculated in (7.7). Thus, we write the volume flow rate in terms of the partial derivative of pressure p w.r.t z as $Q(z,t)=-(sgn\frac{\partial p}{\partial z})\left|\frac{1}{2}\frac{\partial p}{\partial z}\right|^{\frac{1}{n}}\frac{n}{3n+1}h^{\frac{3n+1}{n}}$. By averaging it over a period, we get the time-averaged volume flow rate, $\bar{Q}(z)=\int_0^1 Qdt$. We use the transformation from the laboratory to the wave frame, i.e., $q=Q-h^2$, then the time-averaged volume flow rate takes the form $\bar{Q}(z)=q+\int_0^1 h^2dt$, and hence on substitution $h(z,t)$ from equation (7.19), is given by

$$\begin{aligned}\bar{Q}(z) &= q+1+\epsilon\Big(\frac{2C_1}{\beta}e^{\beta z}(1-e^{-\beta})-e^{k(z-1)}(P_3cos(z-1)+Q_3sin(z-1))\\&+e^{kz}(P_3cosz+Q_3sinz)\Big)+\epsilon^2\Big(-q_2-2(3n+1)C_1^2+\frac{C_1^2}{2\beta}e^{2\beta z}(1-e^{-2\beta})\\&+\frac{2C_2}{\beta}e^{2\beta}(1-e^{-\beta})+C_3e^{2kz}(1-e^{-2k})+2C_1(\frac{n\alpha}{D})\Big(\frac{e^{-\beta(z-1)}}{\beta}(\frac{1}{\beta}-(z-1))\\&-\frac{e^{-\beta z}}{\beta}(\frac{1}{\beta}-z)\Big)-2(\frac{n\alpha}{D})e^{k(z-1)}(P_5cos(z-1)+Q_5sin(z-1))\\&+2(\frac{n\alpha}{D})e^{kz}(P_5cosz+Q_5sinz)+e^{2k(z-1)}(P_8cos2(z-1)+Q_8sin2(z-1))\\&-e^{2kz}(P_8cos2z+Q_8sin2z)+e^{(k+\beta)(z-1)}(P_9cos(z-1)+Q_9sin(z-1))\\&-e^{(k+\beta)z}(P_9cosz+Q_9sinz)\Big),\end{aligned}\tag{7.20}$$

where constants C_3, P_3, P_5, P_8, P_9, Q_3, Q_5, Q_8, and Q_9 are given in appendix.
Now, we write the differential equation, which will determine the contours of the

streamline after getting its solution in terms of flow behavior index n and the wall position h. This can be written in the wave frame of reference under the influence of peristaltic wave propagation along the wall of the elastic oesophageal tube as

$$d\psi = 2RUdR - 2RVdZ. \tag{7.21}$$

Here ψ is the stream function. Under the transformations of axial and radial velocities from the laboratory frame to the wave frame of reference, i.e., $u(r,z,t) = U(R,Z)+1$ and $v(r,z,t) = V(R,Z)$, equation (5.21) takes the form of the exact differential equation by using the equations (7.7) and (7.8). Finally, in the laboratory frame, we write the expression for the stream function as

$$\psi(r,z,t) = r^2\Big(\frac{1}{2}\frac{\partial p}{\partial z}\Big)^{\frac{1}{n}}\Big(\frac{2n}{n+1}\Big)\Big(\frac{n}{3n+1}r^{\frac{n+1}{n}} - \frac{h^{\frac{n+1}{n}}}{2}\Big) - r^2. \tag{7.22}$$

7.3.2 Gaussian forcing applied to a solitary wave

We also take into account the presence of solitary waves traveling along the elastic oesophageal tube due to a spatially localized force represented by $f(z)$. To provide an example, we opt for a Gaussian profile solitary wave force, expressed as $f(z) = e^{-\frac{z^2}{2}}$. In this context, the solution to equation (7.14) can be simplified in Fourier transform terms as follows:

$$H_1(z) = \frac{\iota}{2D\sqrt{\pi}}\int_{-\infty}^{\infty}\left(\frac{\omega}{\beta - \iota\omega}\right)e^{-\omega^2/4}e^{\iota\omega z}dz \tag{7.23}$$

7.4 Results and Discussions

The current investigation aims to examine how the flow of power-law fluid takes place in the considered model of the elastic oesophageal tube. At the same time, we are also looking for the answers to the questions asked in the introduction section. We examine this tube by taking into account the applied force on its wall. The force acting on it from externally to the radial direction. This makes a generation of peristaltic progressive waves along the axial direction through the tube wall. Numerical calculations are made using the regular perturbation method to determine

pressure distribution and volume flow rate distribution along the axial direction of the tube. We also draw the graphs of the contours of the streamline. The plots also show the impacts of dilating forcing amplitudes on these characteristics. Even the presence of shear thinning and thickening due to the considered non-Newtonian fluid model has a large impact on these characteristics as well.

As the bending stiffness parameter D approaches zero, the tube gains infinite flexibility, and the resistance to external forces is solely due to the pressure from the fluid lubrication. In this scenario, the applied force immediately determines the pressure, and equations (7.11) - (7.16) can be solved as straightforward algebraic problems for the tube's radius. To address the discontinuous shocks that may arise, a small amount of stiffness is introduced, as detailed in Appendix A of Takagi and Balmforth's work Takagi and Balmforth (2011), which provides an overview of the key characteristics of solutions when D is significantly smaller than 1.

Conversely, another analytically manageable scenario emerges when the bending stiffness becomes considerably larger, i.e., for $D >> 1$. Under these conditions, the tube's wall can undergo significant deformation only when a corresponding large forcing amplitude is applied, such that $\epsilon \sim D >> 1$. The dominant force balance in the equation $p = D(H-1) + \epsilon e^{kz} f(z)$ then excludes the influence of fluid pressure, implying that the applied force dictates the tube's deformation independently of fluid flow dynamics. This resembles models that specify the wall displacement, as seen in works by Fung and Yih (1968) and Shapiro et al. (1969).

Nevertheless, as explained in Appendix B of Takagi and Balmforth's study Takagi and Balmforth (2011), it is essential to consider the lubrication pressure, except when the tube does not become excessively constricted. If occlusions occur, a different approach is needed to handle the situation.

We set the bending stiffness parameter $D = 1$ and amplitude dilation parameter $k = 0.02$. For the purpose of investigation, we also suppose that the oesophagus accommodates three boluses. This gives us the intuition of concern about the pressure distribution when the propelling of boluses at the cardiac sphincter along the axial wall of the oesophageal tube takes place. As ϵ rises from 0.0045 to 0.0047, we observed that the rise in the curves of the pressure distribution is strengthened at $t = 0$ (Fig. 7.2a). In the same way, the curves show their nature when $t = \pi$, but

this time, its magnitude falls to more negative values due to the relaxation of the supporting muscular wall just behind the bolus (Fig. 7.2b).

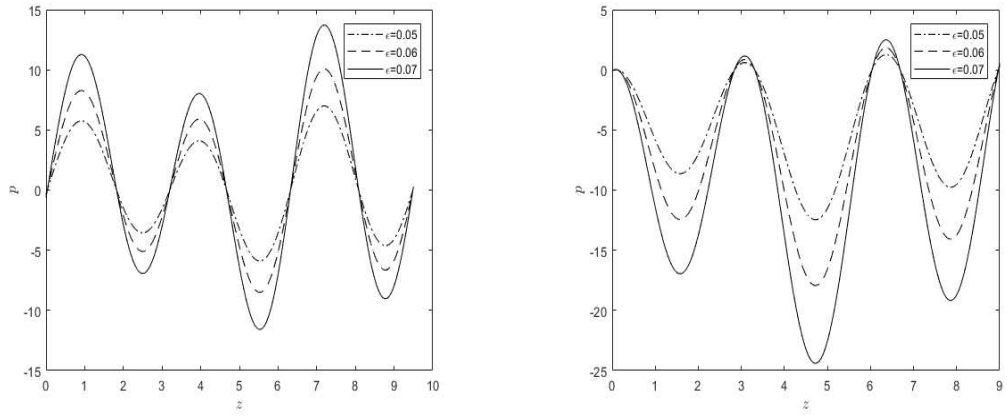

(a) (b)

Figure 7.2: Axial distribution of pressure along the axial length for $\epsilon = 0.05 - 0.07$, other parameters being $k = 0.03$, and $b = 0.03$ for (a) $t = 0$, (b) $t = \pi$.

Furthermore, we observed that due to the effects of dilating forcing amplitude, the behavior of the curves at the crest and trough are highly spiked rather than the other parts when the tube dilated. We see that when the bolus comes into the upper oesophageal sphincter, rolling through the pharynx, the initial pressure requirements are less than till it completely enters. After that, it increases as the boluses progress further. We see the same repetition of this process until a person suffers from some kind of swallowing disorder (such as Achalasia) in the oesophagus.

In Figure (7.3), we observed that variation in pressure for different flow behavior index n of power-law fluid affected its magnitude more. After getting solved, the power law constitutive equation reveals that the pseudoplastic fluids ($n < 1$) require less pressure, and dilatant fluids ($n > 1$) require more pressure than Newtonian fluids. Therefore, as the pseudoplasticity increases, the effect of pressure becomes high, and hence, the pressure distribution profile becomes progressively sharper, which causes an increase in the intensity of propelling boluses forward. This observation is with the agreement of Nicosia and Brasseur (2002), Pandey and Pandey (2024d), Pandey and Pandey (2024b), Pandey and Pandey (2024a), i.e., the pressure

requirement is more at the tail of the bolus when it is subjected towards the cardiac sphincter. Thus, the effect of pressure distribution on the boluses of Newtonian fluid is less than that of dilatant fluid.

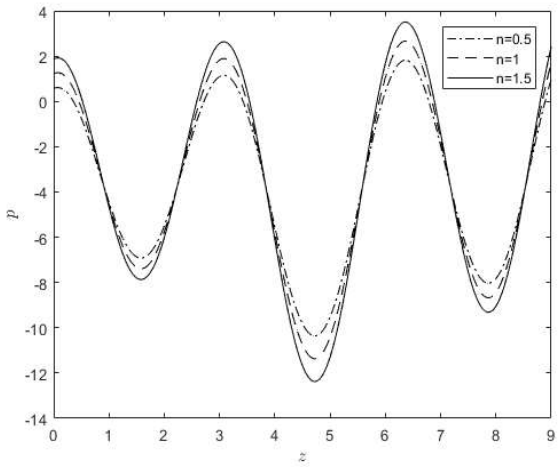

Figure 7.3: The graph displays the distribution of pressure along the axis of an elastic oesophageal tube. The solid, dashed, and dashed-dot curves represent pseudoplastic fluid ($n = 0.5$), Newtonian fluid ($n = 1$), and dilatant fluid ($n = 1.5$), respectively. Here, the fixed parameters are $k = 0.03$ and $b = 0.03$ at $t = 0$.

The plots in the Figure (7.4) have been drawn to know about the change in axial velocity profile with radial positions when dilating, forcing amplitude to increase for two-time instants, i.e., $t = 0$ and $t = 1$. We consider three distinct forcing amplitudes: $\epsilon = 0.0045$, 0.0046, and 0.0047 while keeping $D = 1$. The amplitude dilation parameter is set as $k = 0.02$, i.e., a constant. Our observations reveal two distinct trends in the velocity profile along the radial direction.

As illustrated in Figures (7.4a) and (7.4b), when the forcing amplitudes on the tube are increased, the velocity starts to decrease at $t = 0$ and reaches zero at the tube wall, remaining zero at the axis for each force amplitude. With the passage of time, the velocity gradually regains its original form and becomes higher for lower values of dilating forcing amplitude. This phenomenon suggests that there is no slippage occurring at the tube wall. These findings align with the results presented by Pandey and Singh (2020) for Newtonian fluids.

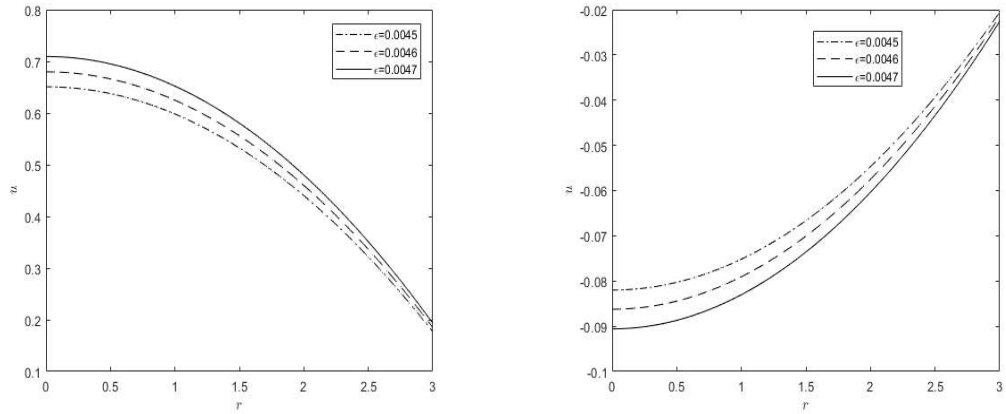

(a) (b)

Figure 7.4: The diagrams display the axial velocity profile along the radial direction for dilating forcing amplitudes ϵ, other parameters being $k = 0.03$, at (a) $t = 0$, and (b) $t = 1$.

In Figure (7.5a), our observations reveal that the velocity magnitude of the dilatant fluid surpasses that of the Newtonian fluid. However, as the fluid transitions from being dilatant to pseudoplastic, we notice that at $t = 0$, the velocity starts to become higher for the Newtonian fluid. Overall, the axial velocity profile demonstrates a decrease along the axial direction. In the case of decreasing dilatancy, the velocity intensity increases. Conversely, when dealing with pseudoplastic fluid, an opposite trend emerges, where the intensity of axial velocity decreases as the fluid's pseudoplasticity increases (Figure 7.5b).

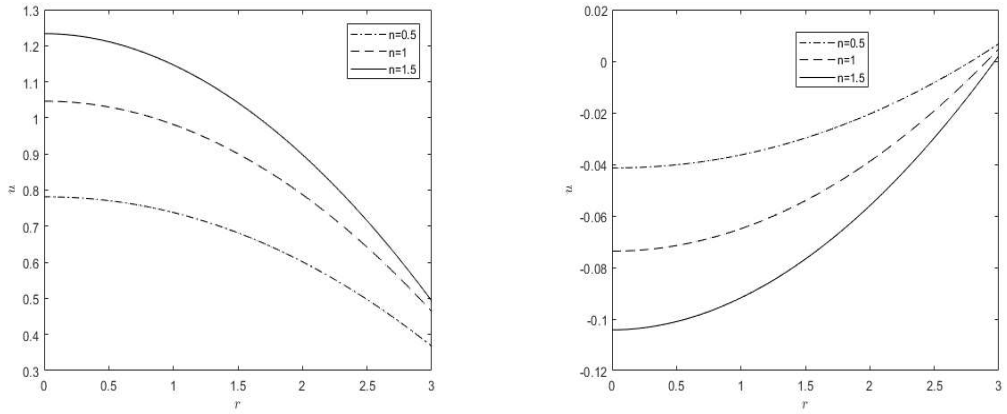

(a) (b)

Figure 7.5: The diagrams display the axial velocity profile along the radial direction for the flow behavior index n, other parameters being $k = 0.03$, at (a) $t = 0$, and (b) $t = 1$.

Three distinct values of forcing amplitude, namely $\epsilon = 0.0045, 0.0046, 0.0047$, are considered while maintaining constants $D = 1$ and $k = 0.02$ (Fig. 7.6). The plots of this figure show how the radial velocity is influenced by the radial forcing amplitude with the tube radius in a non-equilibrium state. We observed that as the application of inward radial forcing at the tube wall gets reduced, the attenuation in the magnitude of the radial velocity can be seen at $t = 0$ (Fig. 7.6a). This approach has positive values. When $t = 1$ (Fig. 7.6b), the grasp of inward radial forcing amplitude strengthens, and the rise in the negative values of the radial velocity starts occurring. This means that the motion of the wall, which is there, started in the transverse direction. This concluded that if the radial velocity started getting positive values, the effects of the dilating forcing amplitude confirmed the propelling of the train of boluses in the forward direction, i.e., along the axial direction of the elastic oesophageal tube.

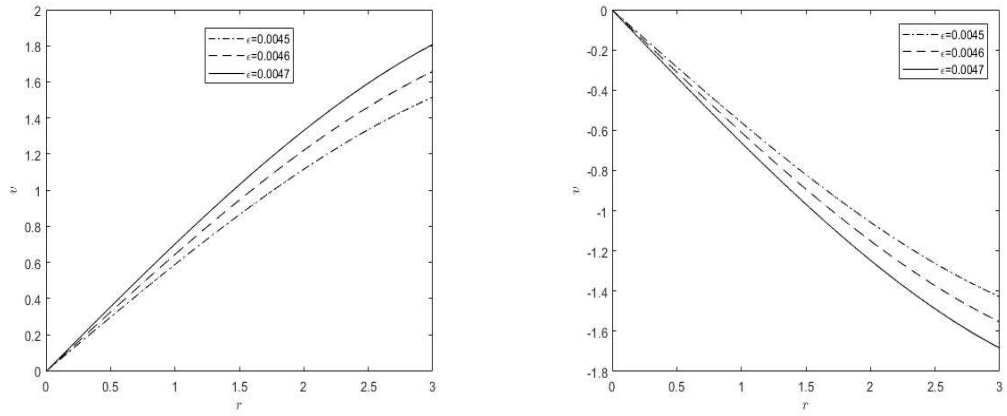

(a) (b)

Figure 7.6: Radial velocity u along the radial direction r for $k = 0.03$, and time instant (a) $t = 0$, and (b) $t = 1$.

In Figure (7.7), we observed that as the flow behavior index n varies from lower to higher values, the radial velocity curves transition from representing pseudoplastic to dilatant fluids, with the highest magnitudes occurring at a radial distance of $r = 3$. This transition from shear-thinning (i.e., decreasing n) to shear-thickening (i.e., increasing n) results in a noticeable attenuation or enhancement in velocity along the radial direction, particularly in the vicinity of the wall (Figure 7.7a).

It's worth noting that for pseudoplastic fluids, an increase in the flow behavior index leads to a distinct reduction in radial velocity at the time instant $t = 1$ (Figure 7.7b). Conversely, for dilatant fluids, an increase in the flow behavior index (i.e., $n > 1$) induces a significant enhancement in velocity magnitude along the radial direction compared to a Newtonian fluid.

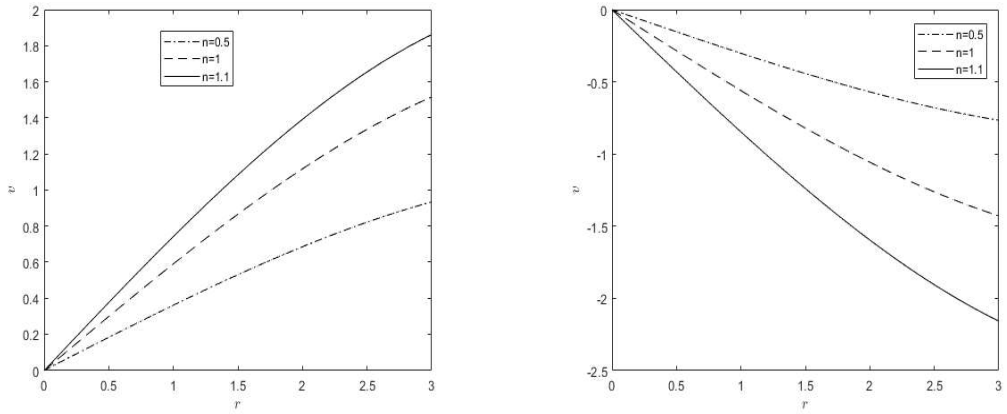

(a) (b)

Figure 7.7: The graphs display the changes with the time instants (a) $t = 0$, and (b) $t = 1$ in the curves of the radial velocity v along the radial direction r for flow behavior index n, other parameters being $k = 0.03$.

Figure (7.8) shows the changes in the wall positions as the transition from shear thickening to shear-thinning of the fluids takes place with time. We observed that the disturbance in the wall position is less in the case of shear-thinning of fluid, whereas the radial velocity $v = \partial h/\partial t$ decreases or increases with the change in the coordinates (h, t), which show that more disturbance with shear-thickening of fluids. Hence, it is noteworthy that the flow behavior index of both shear-thinning and shear-thickening fluids has a notable impact on the wall position. This effect becomes more pronounced as one moves further away from the wall and approaches the boundary region, regardless of the specific flow behavior index considered.

The two different time instances have been discussed here. Beyond the time point $t = 0$, the wall position for pseudoplastic fluids gradually advances from the wall towards the core region. This is indicative of a significant reduction in the flow behavior index n as pseudoplasticity intensifies. In contrast, for dilatant fluids, the wall position progressively diminishes with increasing distance from the wall, specifically after $t = 1.5$ as one moves towards the boundary region.

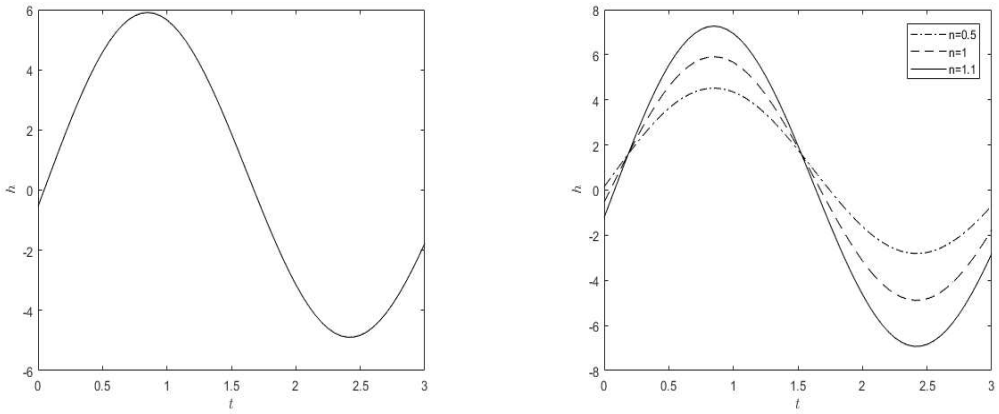

(a) (b)

Figure 7.8: The above two graphs show the behavior of curves, which represent the wall position changing with time for fixed axial position $r = 4$. Also, the curves are given as solid, dashed, and dashed-dotted, representing the pseudoplastic ($n < 1$), Newtonian ($n = 1$), and dilatant ($n > 1$) fluids, respectively. The other parameters are being fixed as $k = 0.02$, $\epsilon = 0.0045, 0.0046, 0.0047$, $D = 1$.

In the plots of Figure (7.9), we discussed the influence of increasing the forcing amplitude that is happening by applying inward radial forcing externally on the boundary wall of the considered elastic oesophageal tube. Due to the large impact with slightly higher values of dilating forcing amplitudes, i.e., $\epsilon << 1$, we set it as $\epsilon = 0.0045, 0.0046, 0.0047$ (for figure (7.9a)) with $D = 1$, $k = 0.02$. We observed that due to the dilating forcing amplitude effects, an increase in the flow rate took place. The magnitude of the flow rate is less when the forcing effect on the boundary wall is less due to the elongation. Whereas it becomes high when the tube goes to its contracted position with the wave propagating along the axial direction. This also aligns with the observation done for the pressure distribution in the figure (7.2a). That is, the increase in the magnitude of pressure distribution when the larger effects of dilating forcing amplitude occur and lower the flow rate along the axial direction of the tube. We also observed that these effects of increasing the pressure at the boundary of the tube wall increase the magnitude of the flow rate for the dilatant fluid ($n > 1$) more in comparison to the Newtonian fluid ($n = 1$), whereas the effects are less when the transition of fluids change from Newtonian to pseudoplastic fluid ($n < 1$). Overall, the net flow is positive.

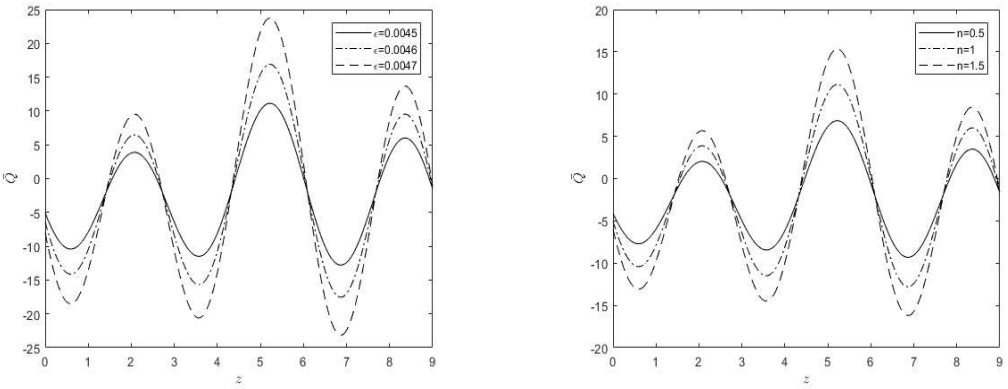

(a) (b)

Figure 7.9: Axial distribution of time-averaged volume flow rate showing the impact of (a) forcing amplitude ϵ, and (b) flow behavior index n, other parameters being $k = 0.02$, $\epsilon = 0.05$, $D = 1$, $t = 0$.

In Figure (7.10), we studied the formation of different patterns of streamline in the laboratory frame when the pressure due to the forcing at the elastic oesophageal tube's boundary wall takes place. For this purpose, we vary the values of dilating forcing amplitude very slightly, i.e., $\epsilon = 0.0045, 0.0046, 0.0047$, and 0.0048. We fixed the other parameters, such as $D = 1$, $k = 0.02$, and $t = 0.0$. Examining these pictures reveals that the presence of the streamlines increases with the increase in the forcing amplitude. On further increasing the ϵ, the central streamlines split into distinct patterns.

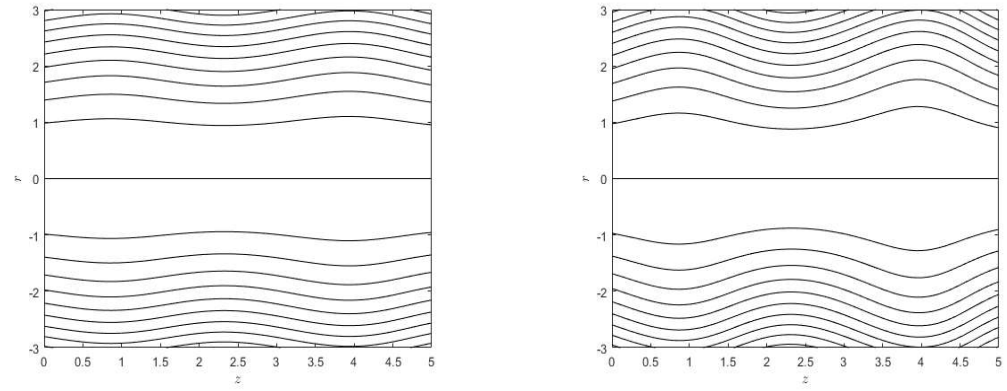

(a) (b)

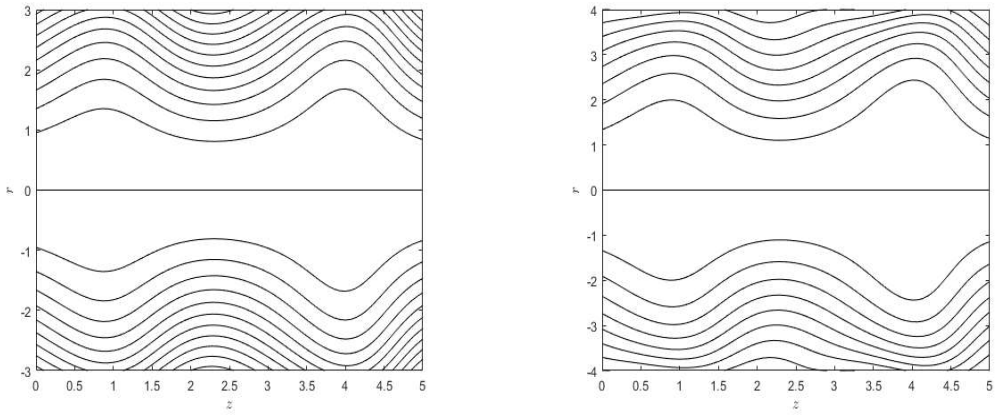

(c) (d)

Figure 7.10: The above plots show a display of an increase in the number of streamlines due to enhancing the forcing on the boundary of the tube wall from externally towards the radial direction. The parameters are set as $k = 0.02$, $D = 1$ for (a) $\epsilon = 0.0045$, (b) $\epsilon = 0.0046$, (c) $\epsilon = 0.0047$ and (d) $\epsilon = 0.0048$.

7.5 Conclusion

We investigate the rheological behavior of a non-Newtonian fluid, typically the power-law model, under the influence of an externally applied force on an elastic oesophageal tube. Our motivation for this study stems from the broad applications of this model in both the biomedical sciences and industrial manufacturing, particularly in the development of prosthetics. We approach this problem through analytical techniques, employing standard methods such as the long wavelength and low Reynolds number approximations. We employ the regular perturbation method to seek solutions in terms of the dilating forcing amplitude denoted as ϵ.

Our investigation encompasses different combinations of forcing wave amplitudes and flow behavior indices spanning various flow parameters that correspond to both shear-thinning and thickening behaviors.

Initially, we focus on how the pressure distribution responds within the system to varying forcing amplitudes. Notably, we observe that as the bolus enters the

oesophagus, less pressure is required due to the relaxation of circular and longitudinal muscles. As we increase the dilating forcing amplitudes, these muscles contract, propelling the bolus's tail forward into the stomach.

We observe that pseudoplastic fluids require less pressure than Newtonian fluids under the same dilating forcing amplitude conditions. Conversely, dilatant fluids necessitate higher pressures to propel boluses into the stomach compared to Newtonian fluids. Consequently, the externally applied force alters the pressure profile, making it sharper and intensifying the propulsion process.

Furthermore, we delve into the impact of dilating forcing amplitude on axial and radial velocity profiles, examining various values of n that correspond to pseudoplastic ($n < 1$), Newtonian ($n = 1$), and dilatant ($n > 1$) behavior of a power-law fluid. Over time, we observe a gradual restoration of velocity to its original form, especially for lower dilating forcing amplitudes, indicating the absence of slippage at the tube wall. However, this phenomenon has a significant effect on the flow rate. Midway through the bolus, the flow rate increases with increasing forcing amplitudes but decreases in the vicinity of contracted regions. Nonetheless, the overall net flow remains positive.

In conclusion, our findings underline how the transition from shear-thinning (i.e., decreasing n) to shear-thickening (i.e., increasing n) behavior in a power-law fluid leads to noticeable alterations in pressure distribution, axial and radial velocity profiles, wall position, and ultimately, flow rate. This study highlights the relevance of non-Newtonian fluids within the context of an elastic oesophageal tube.

Appendix

Constants used in equations (7.16-7.20) are given below:

$$\alpha = (-1)^n n 2^n \Big(\frac{1+3n}{n}\Big)^n,\ \beta = \frac{2\alpha}{D}, \tag{7.24}$$

$$A = \frac{2\beta}{D((k-\beta)^2+1)},\ B = -\frac{2(k^2-k\beta+1)}{D((k-\beta)^2+1)}, \tag{7.25}$$

$$S_1 = \frac{A^2+B^2}{2},\ S_2 = \frac{A^2-B^2}{2},\ S_3 = AB, \tag{7.26}$$

$$P_1 = \frac{A(k-\beta)-B}{(k-\beta)^2+1},\ Q_1 = \frac{B(k-\beta)+A}{(k-\beta)^2+1}, \tag{7.27}$$

$$P_2 = \frac{S_2(2k-\beta)-4S_3}{((2k-\beta)^2+4)},\ Q_2 = \frac{2S_3(2k-\beta)+S_2}{(2k-\beta)^2+4}, \tag{7.28}$$

$$P_3 = \frac{Ak-B}{k^2+1},\ Q_3 = \frac{Bk+A}{k^2+1}, \tag{7.29}$$

$$P_4 = \frac{S_2k-S_3}{k^2+1},\ Q_4 = \frac{S_3k+S_2}{k^2+1}, \tag{7.30}$$

$$P_5 = \frac{P_1k-Q_1}{k^2+1},\ Q_5 = \frac{Q_1k+P_1}{k^2+1}, \tag{7.31}$$

$$P_6 = \frac{P_2k-Q_2}{k^2+1},\ Q_6 = \frac{Q_2k+P_2}{k^2+1}, \tag{7.32}$$

$$P_7 = \frac{(k+\beta)P_3-Q_3}{(k+\beta)^2+1},\ Q_7 = \frac{(k+\beta)Q_3+P_3}{(k+\beta)^2+1}, \tag{7.33}$$

$$P_8 = P_6(3n+1)\beta - \frac{P_4}{2}, Q_8 = Q_6(3n+1)\beta - \frac{Q_4}{2}, \tag{7.34}$$

$$P_9 = 4(3n+1)C_1\beta P_7 - 2C_1P_3',\ Q_9 = 4(3n+1)C_1\beta Q_7 - 2C_1Q_3', \tag{7.35}$$

$$P_3' = \frac{A(k+\beta)-B}{(k+\beta)^2+1},\ Q_3' = \frac{B(k+\beta)+A}{(k+\beta)^2+1}, \tag{7.36}$$

$$C_1 = \frac{2n\alpha}{D}, C_2 = k - \frac{2n\alpha}{D}, C_3 = \frac{S_1}{2k} - \frac{2\alpha(3n+1)S_1}{kD(2k-\beta)}. \tag{7.37}$$

The governing equations are given by

$$\rho\Big(\frac{\partial u}{\partial t} + u\frac{\partial u}{\partial z} + v\frac{\partial u}{\partial r}\Big) = -\frac{\partial p}{\partial z} + \mu\Big(\frac{\partial^2}{\partial r^2} + \frac{1}{r}\frac{\partial}{\partial r} + \frac{\partial^2}{\partial z^2}\Big)u, \tag{7.38}$$

$$\rho\Big(\frac{\partial v}{\partial t} + u\frac{\partial v}{\partial z} + v\frac{\partial v}{\partial r}\Big) = -\frac{\partial p}{\partial r} + \mu(\frac{\partial^2}{\partial r^2} + \frac{1}{r}\frac{\partial}{\partial r} + \frac{\partial^2}{\partial z^2} - \frac{1}{r^2})v, \tag{7.39}$$

$$\frac{1}{r}\frac{\partial}{\partial r}(rv) + \frac{\partial}{\partial z}(u) = 0. \tag{7.40}$$

The non-dimensional variables are
$h' = \frac{H}{a}$, $t' = \frac{ct}{\lambda}$, $v' = \frac{v}{\delta c}$, $r' = \frac{r}{a}$, $k' = \frac{k}{\lambda}$, $p' = \frac{pa^{n+1}}{\lambda\mu c^n}$, $L' = \frac{L}{\lambda}$, $z' = \frac{z}{\lambda}$, $\phi' = \frac{\phi}{a}$, $u' = \frac{u}{c}$,
where $\delta = \frac{a}{\lambda}$, $R_e = \frac{\rho c^{2-n}a^{n+1}}{\mu\lambda}$.

Using the above non-dimensional variables, we write

$$\rho\Big(\frac{\partial cu'}{\partial \frac{\lambda}{c}t'} + cu'\frac{\partial cu'}{\partial \lambda z'} + \frac{ac}{\lambda}v'\frac{\partial cu'}{\partial ar'}\Big) = -\frac{\partial \frac{c\lambda\mu}{a^{n+1}}p'}{\partial \lambda z'} + \mu\Big(\frac{\partial^2}{\partial (ar')^2} + \frac{1}{ar'}\frac{\partial}{\partial ar'} + \frac{\partial^2}{\partial (\lambda z')^2}\Big)cu', \tag{7.41}$$

$$\begin{aligned}\rho\Big(\frac{\partial \frac{ac}{\lambda}v'}{\partial \frac{\lambda}{c}t'} + cu'\frac{\partial \frac{ac}{\lambda}v'}{\partial \lambda z'} + \frac{ac}{\lambda}v'\frac{\partial \frac{ac}{\lambda}v'}{\partial ar'}\Big) = & -\frac{\partial \frac{c\lambda\mu}{a^{n+1}}p'}{\partial ar'} + \mu\Big(\frac{\partial^2}{\partial (ar')^2} + \frac{1}{ar'}\frac{\partial}{\partial ar'} \\ & + \frac{\partial^2}{\partial (\lambda z')^2} - \frac{1}{(ar')^2}\Big)\frac{ac}{\lambda}v',\end{aligned} \tag{7.42}$$

$$\frac{1}{ar'}\frac{\partial}{\partial ar'}(ar'\frac{ac}{\lambda}v') + \frac{\partial}{\partial \lambda z'}(cu') = 0. \tag{7.43}$$

After simplification, the above equations (7.41), (7.42), and (7.43) on using the assumptions of long wavelength and low Reynolds number approximations (i.e., $Re \to 0$, $\delta << 1$ as $\lambda \to \infty$), we write

$$\frac{\partial p}{\partial z} = \Big(sign\frac{\partial u}{\partial r}\Big)\Big[\frac{1}{r}\frac{\partial}{\partial r}\Big\{r\Big|\frac{\partial u}{\partial r}\Big|^n\Big\}\Big], \tag{7.44}$$

$$\frac{\partial p}{\partial r} = 0, \tag{7.45}$$

$$\frac{1}{r}\frac{\partial (rv)}{\partial r} + \frac{\partial u}{\partial z} = 0, \tag{7.46}$$

where $||$ denotes the absolute sign.